



# Monodispersed ultrasmall NiMo metal oxide nanoclusters as hydrodesulfurization catalyst



Rupesh Singh<sup>a</sup>, Deepak Kunzru<sup>a,\*</sup>, Sri Sivakumar<sup>a,b,\*</sup>

<sup>a</sup> Department of Chemical Engineering, Indian Institute of Technology Kanpur, Kanpur 208016, (UP), India

<sup>b</sup> Material Science Programme, DST Thematic Unit of Excellence on Soft Nanofabrication, Centre for Environmental Science & Engineering, Indian Institute of Technology Kanpur, Kanpur 208016, (UP), India

## ARTICLE INFO

### Article history:

Received 18 July 2015

Received in revised form 8 December 2015

Accepted 10 December 2015

Available online 11 December 2015

### Keywords:

Hydrodesulfurization

NiMo/ $\gamma$ -Al<sub>2</sub>O<sub>3</sub>

Dibenzothiophene

Nanocluster

## ABSTRACT

In this study, we report the synthesis of ultrasmall NiMo bimetallic metal oxide nanoclusters (~2 nm), supported on  $\gamma$ -Al<sub>2</sub>O<sub>3</sub> for hydrodesulfurization reaction. The metal oxide nanoclusters were prepared by colloidal synthesis using oleic acid and oleylamine as ligands, followed by incorporation of nanoclusters into the pores of  $\gamma$ -Al<sub>2</sub>O<sub>3</sub>. The nanocluster supported  $\gamma$ -Al<sub>2</sub>O<sub>3</sub> was calcined to remove the ligands followed by sulfidation. Compared to the catalyst prepared using conventional wet impregnation method, the nanoclusters prepared using colloidal synthesis showed enhanced catalytic activity for the hydrodesulfurization of dibenzothiophene because of the ultrasmall size of the metal oxide nanoclusters supported on  $\gamma$ -Al<sub>2</sub>O<sub>3</sub>. In addition, we have evaluated the performance of our catalyst with a diesel sample (containing ~14,700 ppm sulfur) obtained from a crude distillation unit. The sulfur content of the feed was reduced to ~35 ppm at 335 °C and LHSV 2 h<sup>-1</sup> showing the good catalytic activity.

© 2015 Elsevier B.V. All rights reserved.

## 1. Introduction

In recent years, strict environmental regulations on transportation fuel quality have been implemented worldwide to regulate air pollution because of the release of SO<sub>x</sub> from automotive vehicles due to the presence of organosulfur compounds (0.1–5 wt.%) in petroleum feed stocks [1]. Although several methods such as oxidative desulfurization, adsorptive removal, biodesulfurization have been tried for the removal of organosulfur compounds from petroleum stocks, hydrodesulfurization (HDS) is the process used industrially [2]. HDS reaction possesses high activation barrier of the C–S bond hydrogenolysis, which can be reduced by choosing an efficient catalyst, conducting the reaction at elevated temperature (>275 °C) and pressure (>30 bar). Several bimetallic (e.g., NiMo, CoMo, NiW, FeMo, AuMo, RuMo and PtMo) [3–8], and trimetallic (e.g., NiMoW, CoMoW) [9,10] catalysts have been explored for HDS in which MoS<sub>2</sub> is the active phase and Ni, Co, Fe, Au, Ru and Pt are used as promoters. Though several catalysts have been reported in the literature, NiMo bimetallic catalyst is widely used in the industry because of its higher HDS activity. The HDS activity of NiMo is determined by the presence of desired number of Ni atoms at the

edge of MoS<sub>2</sub> lattice which leads to partial filling of the antibonding states causing the reduction in the metal–sulfur bond strength [11]. Catalytic activity of the catalyst can be tuned by controlling the particle size, composition, shape, and nature of metal interaction with the supports (e.g. Al<sub>2</sub>O<sub>3</sub>, MgO, TiO<sub>2</sub>, zeolites, silica, carbon and mesoporous materials) [12–19]. Several reports are available on the preparation of HDS catalysts by different methods, such as the most commonly used wet/incipient impregnation [20–22], chemical vapor deposition, sol–gel synthesis, organic matrix combustion method [23], solid-state ion-exchange method, and hydrothermal method [24]. However, all these methods suffer from the lack of control over the particle size and monodispersity which mainly determines the catalytic activity [25]. In order to control the size and monodispersity, colloidal synthesis using capping agents could be an optimal method [26–29]. Colloidal synthesis approach has several advantages such as control over the composition, size and shape of nanoparticles and the prepared nanoparticles can be easily supported on various matrices (e.g., Al<sub>2</sub>O<sub>3</sub>, MgO, TiO<sub>2</sub>, silica and carbon) [30,31]. There are different reports available in literature for the synthesis of various bimetallic nanoparticles such as PtSn, PtRu, FePt in the size range of (1–10 nm) [32–34]. To the best of our knowledge there is no report available on the synthesis of NiMo metal oxide nanoclusters using colloidal synthesis.

To this end, we report the synthesis of ultrasmall monodispersed NiMo bimetallic metal oxide nanoclusters of size ~2 nm with tailorable composition by colloidal synthesis using oleic acid and

\* Corresponding authors. Fax: +91 512 2590104.

E-mail addresses: [dkunzru@iitk.ac.in](mailto:dkunzru@iitk.ac.in) (D. Kunzru), [srisiva@iitk.ac.in](mailto:srisiva@iitk.ac.in) (S. Sivakumar).

oleylamine as capping agents followed by supporting on  $\gamma$ - $\text{Al}_2\text{O}_3$  support. These ultrasmall metal oxide nanoclusters supported on  $\gamma$ - $\text{Al}_2\text{O}_3$  showed enhanced catalytic activity compared to the widely used impregnation method (called as conventional catalyst) of same composition for the HDS of dibenzothiophene (DBT), which is known to be a refractory sulfur compound present in diesel [35].

## 2. Experimental section

### 2.1. Catalyst preparation

#### 2.1.1. Synthesis of NiMo metal oxide clusters supported on $\text{Al}_2\text{O}_3$ using colloidal approach

All the chemicals used in the present study were of analytical grade and used without further purification. Molybdenum hexacarbonyl (98%), nickel acetylacetonate (95%), oleylamine (70%), trioctylphosphine (97%) and oleic acid (99%) were purchased from Sigma–Aldrich. For the synthesis of NiMo nanoclusters, the required amounts of molybdenum hexacarbonyl ( $\text{Mo}(\text{CO})_6$ ) and nickel acetylacetonate ( $\text{Ni}(\text{acac})_2$ ) were dispersed in 15 ml oleylamine solvent, followed by addition of 0.5 ml oleic acid and 0.5 ml trioctylphosphine (TOP) to this dispersion. Oleylamine acts as a solvent, surfactant as well as a reducing agent whereas oleic acid and TOP were used as co-surfactants to control the growth of metal oxide nanoclusters. The mixture was heated to  $230^\circ\text{C}$  at a heating rate of  $5^\circ\text{C min}^{-1}$  under stirring to nucleate the nanoclusters and kept at this temperature for 10 min. NiMo bimetallic nanoclusters were produced by the decomposition of molybdenum hexacarbonyl and nickel acetylacetonate, in the presence of oleylamine as a ligand, along with oleic acid and trioctylphosphine. The reaction scheme for the synthesis is shown in Scheme 1.  $\text{Ni}(\text{acac})_2$  first forms a complex with oleylamine. The Ni complex and  $\text{Mo}(\text{CO})_6$  thermally decompose at  $\sim 230^\circ\text{C}$  to form metal oxide nanoclusters surrounded by the surfactants. The mixture was then cooled to room temperature followed by addition of acetone to the mixture to precipitate out the particles. The metal oxide nanoclusters were then recovered by centrifugation. NiMo nanoparticles of size  $\sim 10$  nm (NiMo B) has been prepared by increasing the reaction time to 30 min.

The NiMo metal oxide nanoclusters thus obtained were dispersed in *n*-hexane and the required amount of  $\gamma$ - $\text{Al}_2\text{O}_3$  added to the dispersion, keeping the mixture of nanoclusters and  $\gamma$ - $\text{Al}_2\text{O}_3$  under stirring for 6 h, so that the pores of  $\text{Al}_2\text{O}_3$  were filled with the dispersion of the nanoclusters. The slurry was then centrifuged to remove the supernatant. The as-prepared NiMo/ $\gamma$ - $\text{Al}_2\text{O}_3$  was heated at  $100^\circ\text{C}$  for 2 h to remove all the residue volatile compounds (e.g., *n*-hexane) followed by calcination at  $550^\circ\text{C}$  for 2 h. In the calcination step, the surfactant was removed, and the metal species bound to the  $\text{Al}_2\text{O}_3$  surface due to metal support interaction. Li et al. [36] used a similar approach to load PdSn nanoparticles over a carbon support. Catalysts with different NiMo ratios were prepared by varying the amount of precursors. The different catalysts prepared for this study are shown in Table 1. As mentioned in previous reports [3,37], HDS catalyst with Ni/(Ni + Mo) ratio 0.25–0.33 gave the best performance, hence most of the studies were carried out at Ni/(Ni + Mo)  $\sim 0.3$ . These are denoted as NiMo 1–NiMo 4 in Table 1. To check the effect of Ni on HDS activity two catalyst batches (NiMo 5 and NiMo 6) were prepared keeping  $\text{MoO}_3$  loading constant. Similarly, to check the effect of Mo on HDS activity two catalyst batches (NiMo 7 and NiMo 8) were prepared keeping NiO constant.

#### 2.1.2. NiMo metal oxides using wet impregnation method 1

For the sake of comparison, NiMo/ $\gamma$ - $\text{Al}_2\text{O}_3$  was also prepared using incipient wetness impregnation method. For this, 0.578 gm.

of citric acid was dissolved in 2.7 ml of  $\text{H}_2\text{O}$  followed by addition of 0.66 gm of  $(\text{NH}_4)_6\text{Mo}_7\text{O}_{24} \cdot 4\text{H}_2\text{O}$ . The contents were stirred till a clear solution was obtained. Then 0.408 gm of  $\text{Ni}(\text{NO}_3)_2 \cdot 6\text{H}_2\text{O}$  was mixed in the above solution and stirred till it was homogeneously mixed. The solution thus prepared was added drop wise to 3 gm  $\gamma$ - $\text{Al}_2\text{O}_3$  with continuous mixing. Once the precursor salt solution was deposited on  $\gamma$ - $\text{Al}_2\text{O}_3$ , the catalyst sample was dried at  $120^\circ\text{C}$  for 1 h followed by calcination at  $550^\circ\text{C}$  for 2 h. This catalyst has been denoted as NiMo con1. Similarly, NiMo con2 and NiMo con3 were prepared using the same method by varying the precursor salt concentration.

#### 2.1.3. NiMo metal oxides using wet impregnation method 2

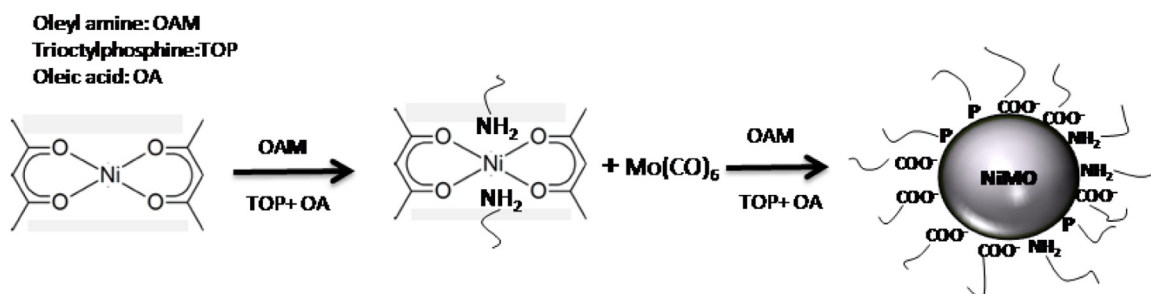
NiMo/ $\gamma$ - $\text{Al}_2\text{O}_3$  catalyst was also prepared using multiple impregnation method, using  $\text{Mo}(\text{CO})_6$  and  $\text{Ni}(\text{acac})_2$  as precursor salts and tetrahydrofuran (THF) as a solvent. For this, 0.31 gm of  $\text{Mo}(\text{CO})_6$  was mixed together in THF. The contents were stirred till a clear solution was obtained. Then 0.19 gm of  $\text{Ni}(\text{acac})_2$  was mixed in the above solution and stirred till it was homogeneously mixed. The solution thus prepared was added drop wise to 1 gm  $\gamma$ - $\text{Al}_2\text{O}_3$  with continuous mixing. Once the precursor salt solution was deposited on  $\gamma$ - $\text{Al}_2\text{O}_3$ , the catalyst sample was dried at  $120^\circ\text{C}$  for 1 h followed by calcination at  $550^\circ\text{C}$  for 2 h. This catalyst has been denoted as NiMo con4. Supported catalysts powder were pelletized, crushed, sieved and the 0.25–0.3 mm size fraction was used for activity test.

### 2.2. Catalyst characterization

Matrix assisted laser desorption/ionization mass spectra was acquired on a time-of-flight mass spectrometer (MALDI-TOF Autoflex II TOF, Bruker Daltonics, Bremen, Germany) equipped with a nitrogen laser ( $\lambda = 337$  nm). Scan accumulation and data processing were performed by using Flex Analysis 3.4 software. FT-IR spectra were recorded on a Spectrum II PerkinElmer instrument in the wave number range of  $600$ – $4000$   $\text{cm}^{-1}$ , using attenuated total reflectance (ATR) with a germanium (Ge) crystal. The spectra and the corresponding data acquisition were automatically obtained using an interfaced computer and a PerkinElmer Spectrum II software package. Two dimensional (2D) surface imaging of film was recorded with an atomic force microscope (AFM, Molecular Imaging Pico-SPM) and was analyzed using data visualization and analysis software (Gwyddion-2.35) for surface morphology parameters, namely (i) root-mean-square roughness ( $R_{\text{rms}}$ ), (ii) average roughness ( $R_{\text{av}}$ ) and (iii) height of growth structure.

The elemental compositions of the prepared NiMo/ $\gamma$ - $\text{Al}_2\text{O}_3$  samples were determined using X-ray fluorescence (XRF). The analysis was done on a Rigaku make ZSX Primus II XRF spectrometer. For XRF analysis, the calcined samples were pelletized using a hydraulic press at a pressure of 15–20 t. For the analysis of Al, the sample was excited using a 100 mA current and a voltage of 30 kV. For Ni and Mo, these values were fixed at 60 mA and 50 kV. The surface area, pore volume, and pore size were determined based on the amount of  $\text{N}_2$  that was adsorbed and desorbed at 77 K, using Autosorb-1C (Model: AS1-C, Quantachrome, USA). X-Ray Diffraction (XRD) was performed on a PAN analytical make X-ray diffractometer using Ni filtered  $\text{K}\alpha$  radiation from a Cu target ( $\lambda = 1.541841$  Å). The sample was scanned between the angles  $10^\circ$ – $80^\circ$  at a scan rate of  $3^\circ/\text{min}$ .

The TEM analysis of the unsupported and  $\gamma$ - $\text{Al}_2\text{O}_3$  supported NiMo samples was carried out on FEI make TecnaiTM G2 U-Twin (200 kV) transmission electron microscope equipped with EDS detector. For TEM analysis, the samples were dispersed in *n*-hexane. 5  $\mu\text{l}$  of the sample was loaded on a carbon-coated copper grid which



**Scheme 1.** Synthesis of NiMo bimetallic metal oxide nanoclusters by colloidal synthesis.

**Table 1**

Composition and surface area of the different NiMo nanocatalysts supported on  $\gamma$ -Al<sub>2</sub>O<sub>3</sub>.

	Al <sub>2</sub> O <sub>3</sub> wt. %	MoO <sub>3</sub> wt. %	NiO wt. %	Surface area (m <sup>2</sup> /g)	Pore volume (cm <sup>3</sup> /g)	Pore size (nm)
Al <sub>2</sub> O <sub>3</sub>	–	–	–	201.3	0.61	7.75
NiMo 1	82.0	13.2	4.8	137.7	0.39	5.30
NiMo 2	83.8	11.9	4.3	137.8	0.40	5.30
NiMo 3	90.1	7.5	2.4	139.7	0.40	5.37
NiMo 4	93.9	4.5	1.6	147.3	0.42	5.67
NiMo B	82.1	13.4	4.5	125.3	0.36	4.93
NiMo 5	85.4	13.3	1.1	141.8	0.42	5.46
NiMo 6	78.2	13.1	8.5	131.7	0.38	5.07
NiMo 7	77.7	17.8	4.5	129.5	0.38	4.99
NiMo 8	90.1	5.6	4.3	150.4	0.44	5.79
NiMo con1	81.4	13.8	4.8	146.3	0.42	5.63
NiMo con2	76.3	18.4	5.3	128.1	0.36	4.93
NiMo con3	91.1	6.8	2.1	153.2	0.43	5.90
NiMo con4	82.9	12.6	4.5	141.3	0.41	5.44

was dried under vacuum. The average metal oxide nanocluster (Size<sub>avg</sub>) was calculated according to following equation:

$$\text{Size}_{\text{avg}} = \frac{\sum_{i=1}^n n_i d_i}{\sum_{i=1}^n n_i} \quad (1)$$

In Eq. (1)  $n_i$  is the number of nanoclusters with size  $d_i$ . Calculations were performed by taking five images which includes ~50 nanoclusters each.

The average slab length ( $L_{\text{avg}}$ ) and stacking number ( $N_{\text{avg}}$ ) were calculated according to following equations:

$$L_{\text{avg}} = \frac{\sum_{i=1}^n n_i l_i}{\sum_{i=1}^n n_i}; N_{\text{avg}} = \frac{\sum_{i=1}^n n_i N_i}{\sum_{i=1}^n n_i} \quad (2)$$

where  $n_i$  are the number of stacks of length  $l_i$ , and  $N_i$  is the number of layers in the cluster.

To determine the reducibility of the material, the TPR analysis of the supported catalyst sample was performed on the Quantachrome instrument. TPR was performed using 5% (v/v) H<sub>2</sub> in N<sub>2</sub>. Prior to analysis, the sample was degassed in He flow at 200 °C for 2 h. The sample was then cooled to room temperature in the presence of an inert gas. Then, 5% H<sub>2</sub> in N<sub>2</sub> was introduced at 10 ml/min for 30 min in the reactor at ~40 °C. The sample temperature was continuously raised from 40 °C to 1000 °C at 15 °C/min. The amount of hydrogen consumption was recorded by a thermal conductivity detector (TCD).

The Raman spectra of the fresh and spent catalysts were recorded using a Raman spectrometer (Senterra, Bruker Optik GmbH). An Ar-ion laser having a wavelength of 532 nm was used for

excitation. 2 mW of laser power was used to obtain the Raman spectra. Scanning electron microscopy image of the supported NiMo 2 sample was taken on Carl Zeiss (NTS GmbH-SUPRA 40VP) equipment, equipped with X-ray energy-dispersive (EDX) microanalyzer.

### 2.3. Catalyst activity test

The sulfided form of the NiMo/ $\gamma$ -Al<sub>2</sub>O<sub>3</sub> catalyst is known to be the active form of the hydrosulfurization catalyst. Therefore, before evaluating the HDS activity of the catalyst, the catalyst was sulfided. The same experimental set-up was used for sulfiding as well as for the HDS activity test, and a schematic diagram of the experimental set-up is shown in Fig. 1. The set-up consisted of a feeding section, reactor unit and the sample collection unit. The liquid was fed by a high pressure metering pump and mixed with the gases before the reactor inlet. The flow of inlet gases (hydrogen, helium) was regulated by mass flow controllers. The stainless steel reactor tube (i.d.: 3.2 mm; length: 300 mm) was mounted vertically in a furnace of 270 mm length. The catalyst bed temperature was measured using a chromel–alumel thermocouple which was in direct contact with the catalyst bed. The reactor effluent was cooled in a condenser in which a refrigerated coolant was circulated. The reactor pressure was maintained by a back pressure regulator (BPR) installed after the condenser. The cooled reactor effluent from the BPR was routed through a gas–liquid separator. The liquid product was collected for analysis and the non-condensables vented. The liquid sample was analyzed on a gas chromatograph equipped with Petrocol DH capillary column (100 m × 0.25 mm) using FID detector. Nitrogen was used as the carrier gas.

The catalyst was sulfided using 10 wt.% of dimethyl disulfide (DMDS) dissolved in *n*-heptane. The sulfiding protocol was as follows: (i) the catalyst temperature was first increased at atmospheric pressure from 25 °C to 150 °C in 120 min under a helium flow of 30 cm<sup>3</sup>/min; (ii) when the temperature reached 150 °C, the helium flow was reduced to zero and the reactor pressure gradually increased by feeding hydrogen at a flow rate of 100 ml/min.

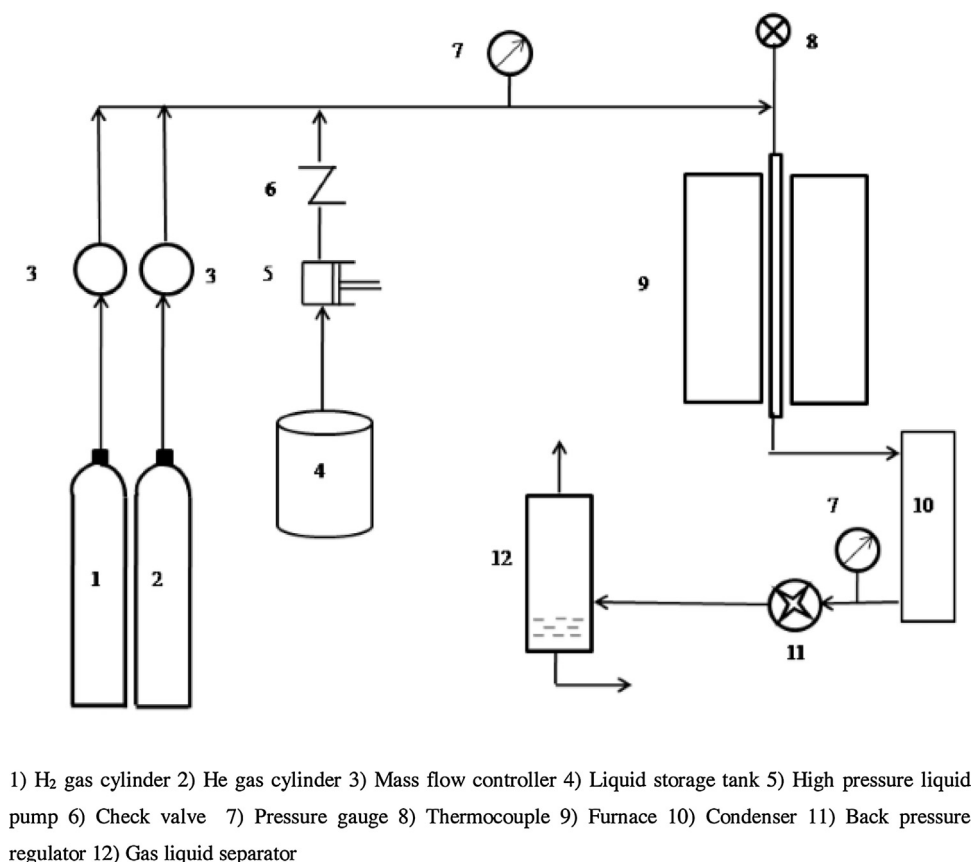


Fig. 1. Schematic diagram of the hydrodesulfurization set-up.

The sulfiding feed (0.17 ml/min) was started when the reactor pressure had reached 10 bar. Under the combined flow of liquid and hydrogen, the reactor pressure was further increased to 30 bar. The catalyst was kept at this temperature for 60 min; (iii) the temperature was then increased from 150 °C to 230 °C in 120 min and the catalyst kept at this temperature for 180 min; (iv) the catalyst temperature was increased from 230 °C to 340 °C in 120 min and kept at this temperature for 10 h.

After sulfiding, the HDS activity of the catalyst was investigated at 30 bar pressure in the temperature range of 275–335 °C. The liquid feed was 1.68 wt.% DBT in *n*-decane (corresponding to 2920 ppm sulfur in feed). For all the runs, mass of catalyst used was 150 mg, the flow rate of hydrogen was 110 ml/min and the flow rate of liquid was varied between 0.1–0.3 ml/min. The catalyst was stabilized for at least 1 h before acquiring the conversion data. Catalytic activity for NiMo 2 catalyst was also checked using 4,6-dimethyl dibenzothiophene (4,6-DMDBT) in decalin solvent. All the reaction conditions were kept same as those for the DBT runs. In addition, the performance of NiMo 2 was also evaluated with a diesel sample obtained from the crude distillation unit of an Indian refinery at 335 °C and a LHSV of 2 h<sup>-1</sup>. The sulfur content of the diesel was 14775 ppm sulfur and the boiling range was 206–368 °C.

### 3. Results and discussion

#### 3.1. Synthesis of NiMo nanoclusters supported on Al<sub>2</sub>O<sub>3</sub>

A four step methodology was followed to prepared ultra small NiMo metal oxide nanoclusters supported on  $\gamma$ -Al<sub>2</sub>O<sub>3</sub>. First, the NiMo metal oxide nanoclusters were prepared using colloidal co-precipitation method by decomposing the metal precursors in presence of oleylamine, oleic acid and trioctylphosphine

surfactants at high temperature. The prepared metal oxide nanoclusters were then dispersed in *n*-hexane and incorporated in the pores of  $\gamma$ -Al<sub>2</sub>O<sub>3</sub>. The nanoclusters supported on  $\gamma$ -Al<sub>2</sub>O<sub>3</sub> were calcined to remove the ligands. Finally, the supported metal oxide nanoclusters were sulfided with dimethyl disulfide to form the sulfided phase, which is considered to be the active phase for hydrodesulfurization reaction. The metal content could be tuned by varying the concentration of the metal precursors and the size of the synthesized particles could be controlled by varying the reaction time. To check the effect of reaction time on the size of nanoclusters, the reaction time was increased from 10 to 30 min, keeping the MoO<sub>3</sub> content and Ni/(Ni + Mo) ratio the same.

#### 3.2. Catalyst characterization

As shown in Fig. 2, the size of the metal oxide nanoclusters increased from ~2 nm to ~10 nm when the reaction time was increased from 10 to 30 min. This increase in size is due to the tendency of the metal oxide nanoclusters to aggregate with aging time beyond a critical time. The TEM image shows that the synthesized unsupported NiMo metal oxide nanoclusters after a reaction time of 10 min were highly monodisperse, with average size of 2.1 nm. The AFM image (Supplementary material, Fig. S1) of the unsupported NiMo metal oxide nanoclusters also support the presence ~2 nm size crystallites. AFM image shows some physically agglomerated clusters which are due to the effect of drying. The size of the clusters is controlled by the surfactants which act as stabilizers for the nanocluster by hindering their growth through Ostwald ripening.

The FTIR spectra of the synthesized nanocluster shows bands at 3358 cm<sup>-1</sup>, 2926 cm<sup>-1</sup>, 2846 cm<sup>-1</sup> and 1640 cm<sup>-1</sup> (Fig. 3). The bands at 2926 and 2846 cm<sup>-1</sup> in unsupported NiMo sample were assigned to the asymmetric (V<sub>as</sub>) and symmetric (V<sub>s</sub>) stretching

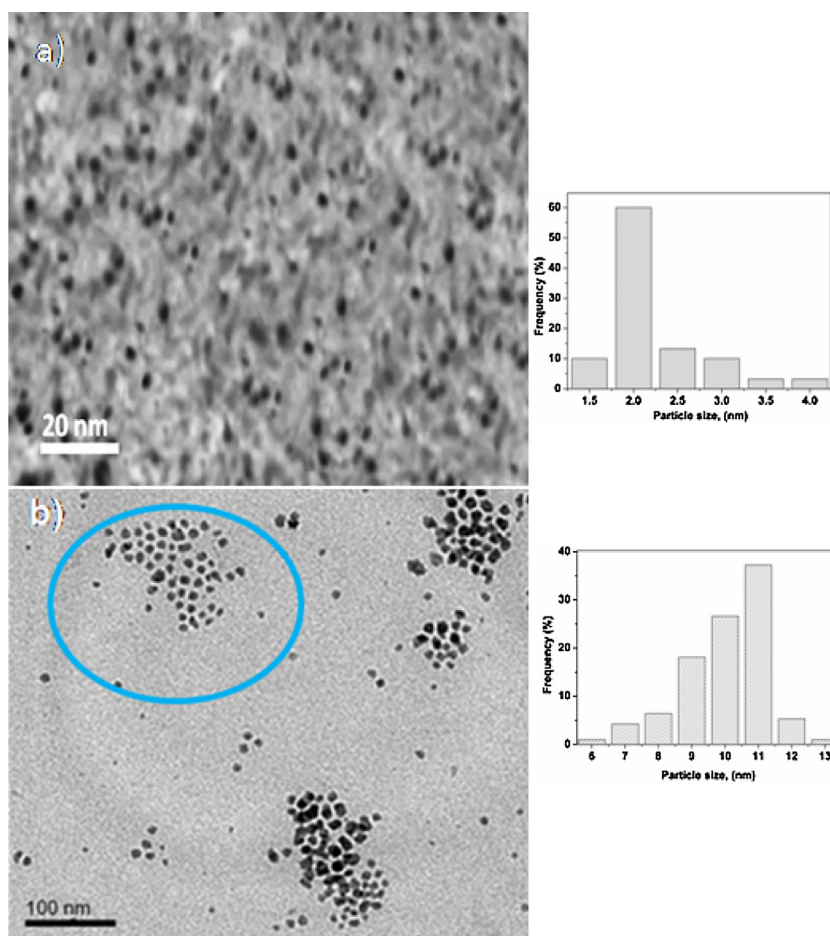


Fig. 2. TEM image of unsupported NiMo metal oxide nanoclusters/nanoparticles by varying the reaction time: (a) 10 min and (b) 30 min.

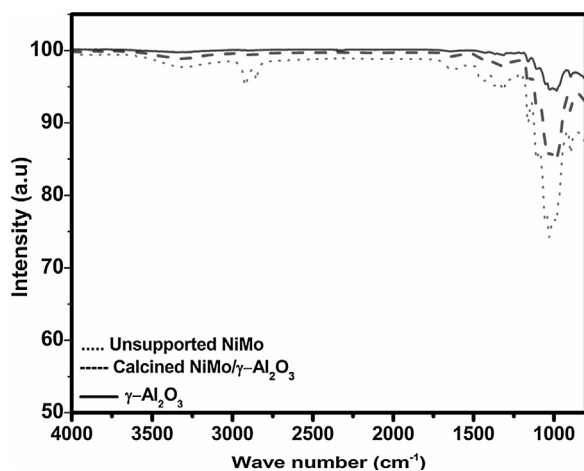


Fig. 3. FTIR spectra of unsupported NiMo nanocluster, NiMo1 (supported on  $\gamma$ - $\text{Al}_2\text{O}_3$ ) and bare  $\gamma$ - $\text{Al}_2\text{O}_3$ .

vibrations of methylene ( $\text{CH}_2$ ). The band at  $1640\text{ cm}^{-1}$  is due to the presence of ( $\text{C}=\text{O}$ ) group. The broad band at  $3358\text{ cm}^{-1}$  was attributed to the presence of  $-\text{OH}$  stretch present in carboxylic acid. This implies that the oleic acid is attached to the nanocluster surface due to its strong ligand nature in comparison to oleylamine. Thus, oleic acid surfactant tends to bind with surface metal atoms during the growth process, thereby blocking the active sites for the catalytic surface reaction [38]. Therefore, it is necessary to remove the surfactant from these metal oxide nanoclusters. The

surfactant was removed by calcination after supporting these metal oxide nanoclusters on the  $\gamma$ - $\text{Al}_2\text{O}_3$  support. A thermogravimetric analysis was done to determine the minimum calcination temperature for complete removal of the surfactant from the metal oxide nanoclusters. The thermogravimetric analysis of the unsupported NiMo nanocluster (Supplementary material, Fig. S2) showed that with an increase in temperature there was a gradual weight loss for sample till  $500^\circ\text{C}$ . Beyond  $500^\circ\text{C}$ , no weight loss was observed. This suggests that the removal of the surfactant is complete at  $500^\circ\text{C}$ . This was also confirmed using FTIR analysis. FTIR analysis of the calcined sample (Fig. 3) shows the disappearance of characteristic peaks at  $2926\text{ cm}^{-1}$ ,  $2846\text{ cm}^{-1}$  and  $1640\text{ cm}^{-1}$ , confirming the removal of surfactant molecules.

MALDI-TOF can be used to characterize ultrasmall nanoparticles. The mass spectra obtained by MALDI-TOF is given in the Supplementary material (Fig. S3). This shows a peak at 1031 ( $m/z$ ) suggesting the formation of  $\text{Ni}_2\text{Mo}_6\text{O}_{20}$  (Mol. wt. = 1013) containing a molecule of water (calculated total molecular weight along with water = 1031).

For determining the HDS activity of the synthesized metal oxide nanoclusters, these were supported on  $\gamma$ - $\text{Al}_2\text{O}_3$ . The specific surface area, pore size and pore volume of the synthesized catalyst samples were determined using nitrogen adsorption-desorption and are listed in Table 1. Compared to pure  $\gamma$ - $\text{Al}_2\text{O}_3$ , the surface area, pore size and pore volume decreased significantly due to the metal loading. The elemental composition of the prepared samples was determined using XRF and the results are given in Table 1. Earlier studies have reported that the optimum ratio of  $\text{Ni}/(\text{Ni} + \text{Mo})$  for HDS catalysts is between 0.25–0.33 [3]. The XRD

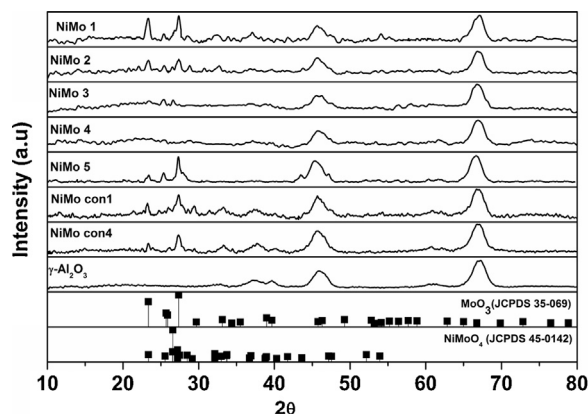


**Fig. 4.** XRD patterns of NiMo metal oxide nanoclusters supported on  $\gamma$ -Al<sub>2</sub>O<sub>3</sub> and NiMo catalysts prepared using wet impregnation method (NiMo con1 and NiMo con4).

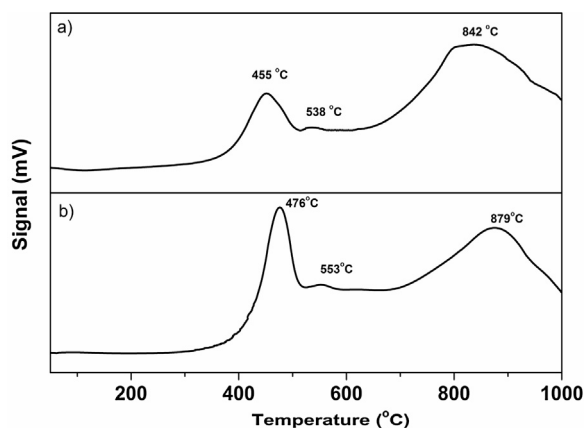


**Fig. 5.** TPR profile of the NiMo/ $\gamma$ -Al<sub>2</sub>O<sub>3</sub> catalyst (a) NiMo 1; (b) NiMo con1.

data of the NiMo nanocluster supported on  $\gamma$ -Al<sub>2</sub>O<sub>3</sub> with different metal loading along with NiMo con1 and NiMo con4 catalysts are shown in Fig. 4. The XRD analysis shows the major phase present was MoO<sub>3</sub> and the minor phase was NiMoO<sub>4</sub>. Comparing the profiles for NiMo 1–NiMo 4, it can be seen that for a fixed Ni/(Ni + Mo) ratio of  $0.3 \pm 0.02$ , with a decrease in metal loading, the intensity of diffraction peaks decreased. The prominent diffraction peaks at  $2\theta = 23.14^\circ$  and  $26.99^\circ$  correspond respectively to (1 1 0) and (0 2 1) planes of MoO<sub>3</sub> orthorhombic phase and the peaks at  $2\theta = 26.64^\circ$  and  $37.04^\circ$  correspond to (1 0 0) and (4 0 0) planes of NiMoO<sub>4</sub> monoclinic phase. The two prominent broad diffraction peaks that appeared at  $2\theta = 46^\circ$  and  $67^\circ$  were assigned to  $\gamma$ -Al<sub>2</sub>O<sub>3</sub> which was used as the support to disperse the synthesized NiMo metal oxide nanoclusters. XRD analysis also indicates the presence of MoO<sub>3</sub> as major phase and NiMoO<sub>4</sub> as a minor phase in case of NiMo con1 and NiMo con4 catalysts. SEM-EDX images of NiMo 2 catalyst (Supplementary material, Fig. S4), shows the distribution of Ni and Mo species on the alumina support. The red and green dots represent Mo and Ni species, whereas alumina surface is represented in dark color. Image confirms the homogeneous distribution of Ni and Mo species on the alumina support, with no evidence of aggregate formation.

The comparative TPR analysis for NiMo/ $\gamma$ -Al<sub>2</sub>O<sub>3</sub> catalyst prepared using colloidal synthesis NiMo 1 with the catalyst prepared by incipient wetness impregnation method (NiMo con1) is shown in Fig. 5. The reduction profile of NiMo 1 shows hydrogen consumption in a broad temperature interval (between 400 and 1000 °C) with two main reduction peaks at 455 °C and 842 °C. The lower

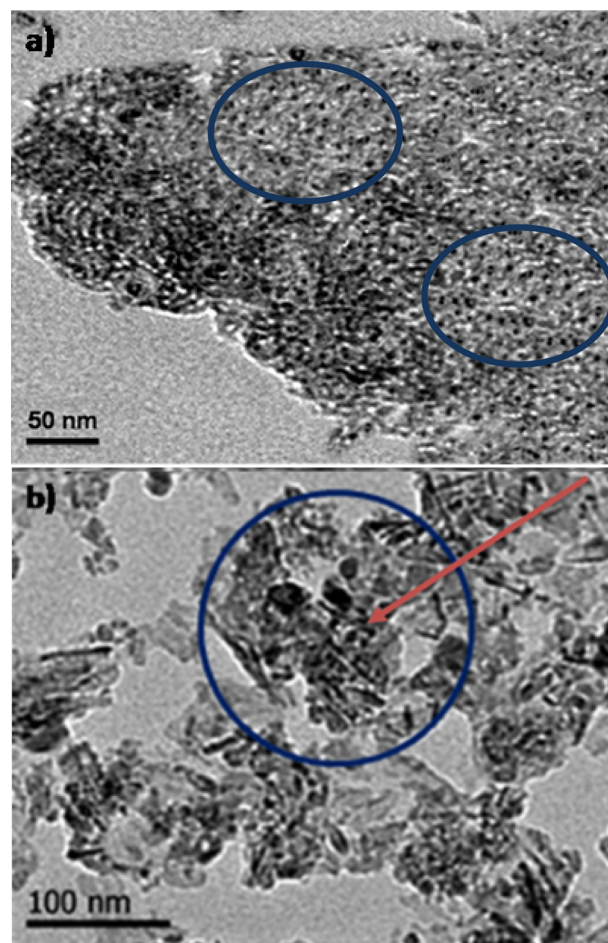


**Fig. 6.** TEM image of NiMo nanoclusters supported on Al<sub>2</sub>O<sub>3</sub> (a) NiMo1 and (b) NiMo con1.

temperature peak (455 °C) can be attributed to the first step of reduction (from Mo<sup>6+</sup> to Mo<sup>4+</sup>). The peak at 842 °C can be ascribed to the reduction of Mo<sup>4+</sup> to Mo<sup>0</sup> [39–42]. Similarly, two main reduction peaks were observed for NiMo con1, with a shift in reduction positions toward higher temperature. The shift in first and second reduction peaks was 21 °C and 37 °C, respectively. The TPR results shows that Ni-promoted MoO<sub>3</sub> nanoclusters prepared using colloidal synthesis are more reducible in comparison to NiMo con1. NiMo 1 showed a small reduction peak at 538 °C due to the reduction of Ni<sup>2+</sup> to Ni<sup>0</sup>. This peak shifted to 553 °C for NiMo con1.

The TEM analysis was also done for the  $\gamma$ -Al<sub>2</sub>O<sub>3</sub> supported NiMo metal oxide nanoclusters and the TEM image of the calcined NiMo 1 is shown in Fig. 6a. Comparing Figs. 6a and 2a, it can be seen that the size of the metal crystallites on the supported catalyst were in the same range as those of unsupported catalyst, implying that the crystallite did not increase during calcination. Even for the highest Mo loading, there was no noticeable physical agglomeration of nanoparticles during loading onto the support and subsequent calcination at 550 °C. Fig. 6b shows the TEM image of NiMo con1 catalyst of the same metal loading prepared by wet impregnation method. For this catalyst, the size of the nanoparticles is bigger with a high degree of polydispersity compared to NiMo 1.

It is well established that the active species for HDS is the NiMoS phase with Ni on the edges of the MoS<sub>2</sub> slabs. The slab length and the stacking number can influence the catalytic activity. In order to investigate the slab length and stacking number TEM analysis of sulfided NiMo 1 and sulfided NiMo con1 were carried out (Fig. 7). TEM images along with histogram of sulfided NiMo 1 and sulfided

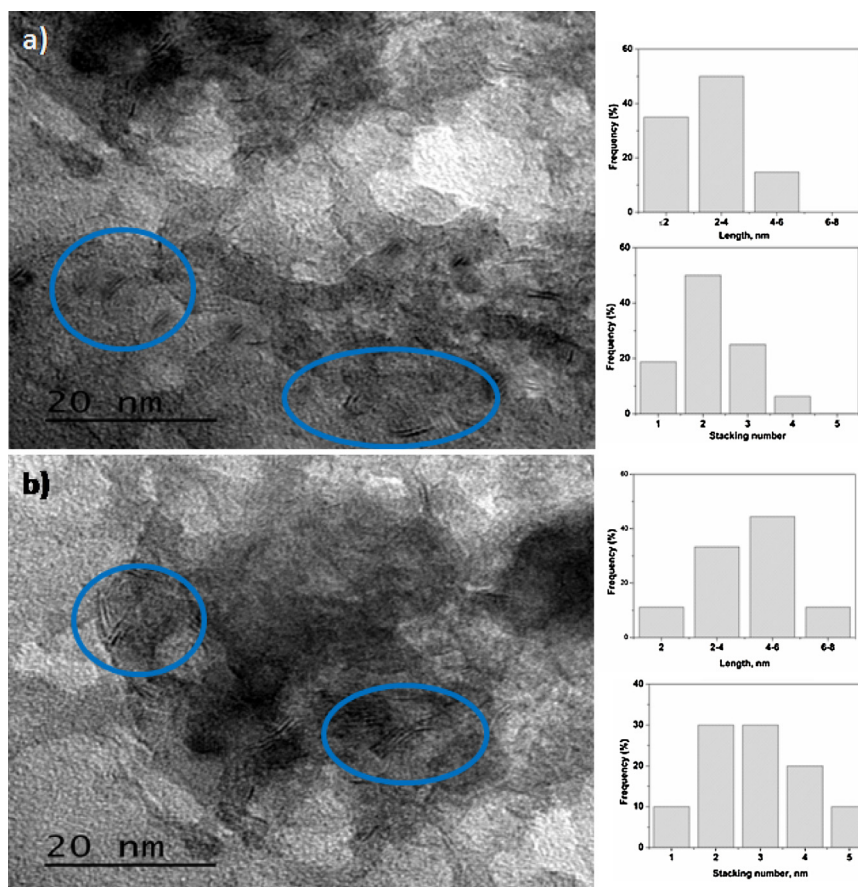


Fig. 7. TEM image of sulfide NiMo/ $\gamma$ -Al<sub>2</sub>O<sub>3</sub> (a) NiMo1 and (b) NiMo con1.

NiMo con1 clearly shows the presence of layered structure suggesting the presence of sulfided active phase which matches with earlier reports [43]. Further, it is evident from TEM images that average slab length of sulfided NiMo 1 (~2.6 nm) is lesser compared to sulfided NiMo con1 (~3.7 nm). In addition, the average stacking number of sulfided NiMo 1 (~2) is lesser compared to sulfided NiMo con1 (~3).

### 3.3. Catalyst activity

Due to its low reactivity for HDS, dibenzothiophene was chosen as the model refractory sulfur compound for testing the catalytic activity of the prepared catalysts. The catalytic activity of the NiMo/ $\gamma$ -Al<sub>2</sub>O<sub>3</sub> catalysts prepared using colloidal synthesis was compared at identical conditions with catalysts prepared using incipient wetness impregnation (NiMo con1 and NiMo con4, Table 1). Preliminary runs were performed to check the importance of external and pore diffusional resistances on the rate of reaction. These experiments showed that pore diffusional resistances were not present for an average catalyst size smaller than 0.32 mm. Therefore, for all the runs, the average catalyst size used was 0.275 mm. Runs made at a constant  $W/F_{A0}$  of  $2.38 \times 10^2$  kg cat.h/kmol DBT and different inlet liquid feed rates (0.1–0.3 ml/min) confirmed that for the flow rates used in this study external mass transfer resistances did not affect the rate of reaction.

The effect of temperature, flow rate and MoO<sub>3</sub> loading at Ni/(Ni + Mo) ~0.3 on the activity and selectivity of the catalysts was investigated. The variation of conversion of DBT with temperature at a  $W/F_{A0}$  of  $2.38 \times 10^2$  (kg cat.h/kmol DBT) is shown in Fig. 8a. As expected, in each case, the conversion increased with temperature. Beyond 320 °C, the increase in conversion was marginal. As can be

seen from this figure, NiMo 1 and NiMo 2 catalysts had a higher catalytic activity compared to the conventional catalysts (NiMo con1 and NiMo con4), especially at lower temperatures (275–305 °C). It should be noted that the MoO<sub>3</sub> loading on NiMo 2 was lower than that of the conventional catalyst. At higher temperature (>305 °C), the conversions obtained with NiMo 1, NiMo 2 and the conventional catalysts were >98%. At high conversion, the sulfur content of the desulfurized product stream was also measured using XRF. At 320 °C, the sulfur content in the product stream was 30 ppm for NiMo 2 catalyst in comparison to a sulfur content of 76 ppm obtained with NiMo con1. The variation of DBT conversion with MoO<sub>3</sub> loading at 305 °C is shown in Fig. 8b. Till a MoO<sub>3</sub> loading of 11.9 wt.%, the conversion of DBT increased with metal loading, but beyond this loading, not much change in catalytic activity was observed. Similar results were obtained with NiMo/ $\gamma$ -Al<sub>2</sub>O<sub>3</sub> catalysts prepared by impregnation method. The variation of conversion with temperature for these catalysts is shown in Fig. S5 (Supplementary material). As observed with catalysts prepared by colloidal synthesis, at high MoO<sub>3</sub> loading, the conversion decreased. Two major models (rim-edge and brim site) have been proposed to explain the activity and selectivity of HDS catalysts [44]. Both the models result in a similar structure–function relationship. In the rim edge model [45], rim sites (top and bottom layers) are assumed to catalyze the hydrogenation and direct desulfurization (C–S bond cleavage) while the edge sites (interior layers) are responsible for direct desulfurization. Berhaut et al. [46] extended this model for supported catalysts and included two type of sites for each, they examined the effect of MoS<sub>2</sub> slab morphology and the metal–support interaction on the activity and selectivity of HDS catalysts. They proposed two different types in which metals at type I site are relatively difficult to reduce since these posses

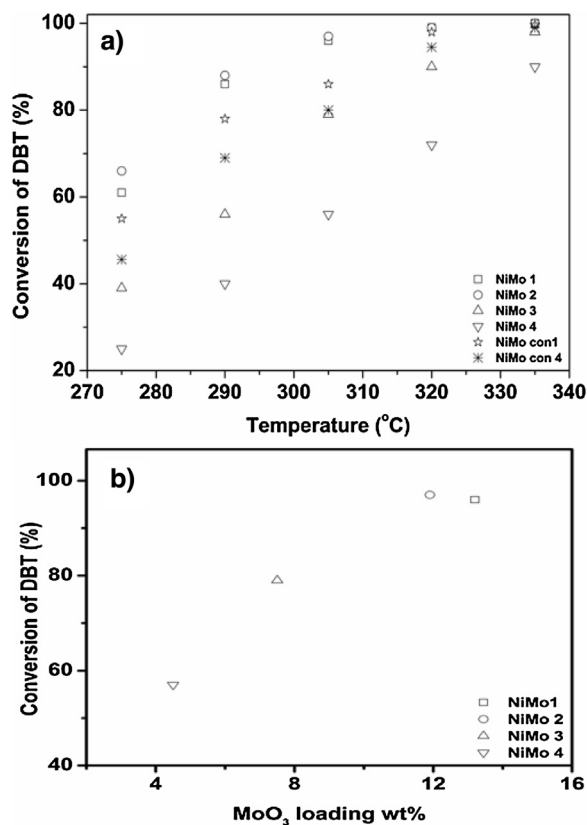


Fig. 8. Effect of reaction temperature and MoO<sub>3</sub> loading on the conversion of DBT ( $W/FA_0 = 2.38 \times 10^2$  kg cat.h/kmol DBT) (a) effect of temperature and (b) effect of MoO<sub>3</sub> loading (Temperature = 305 °C).

strong metal–support interaction whereas metals at type II are relatively easy to reduce because of weaker metal–support interaction. In addition, they proposed that sulfur vacancies formed on both rim and edge sites play a key role in providing active sites for adsorption of reactants. The formation of vacancies depends on the strength of Mo–O–Al linkages between the metal and support.

We believe that the possible reasons behind the enhanced activity of the current colloidal synthesized catalysts are: (i) presence of smaller slabs and lesser number of stacks of sulfide phase compared to catalyst prepared using conventional wet impregnation method favoring the formation of more edge and rim sites (confirmed by TEM images) and (ii) easier reducibility of the catalysts (supported by TPR result) compared to catalyst prepared using conventional method that would favor the formation of more sulfur vacancies, possibly the type II sites.

To check the efficacy of the most active catalyst (NiMo 2), runs on this catalyst and conventional catalyst (NiMo con1) were also taken with 4,6-dimethyl dibenzothiophene (4,6-DMDBT) and a diesel sample obtained from crude distillation unit of an Indian refinery. The variation of conversion of 4,6-DMDBT with temperature for both the catalysts is shown in Fig. S6. Similar to DBT, NiMo 2 had a higher activity for HDS of 4,6-DMDBT, especially at lower temperatures (275–305 °C). The conversion increased with temperature and for NiMo 2 was 66.5% at 335 °C, which was lower than the conversion obtained with DBT at identical conditions. 4,6-DMDBT is known to be more refractory than DBT because of the presence of alkyl groups at 4 and 6 position, which obstruct the interaction of the sulfur atom with the active sites [47]. Even with the diesel feed, NiMo 2 was more active than NiMo con1. At 335 °C and a LHSV of 2 h<sup>-1</sup>, the sulfur content reduced from 14775 ppm to 34 ppm for NiMo 2 and to 84 ppm for NiMo con1.

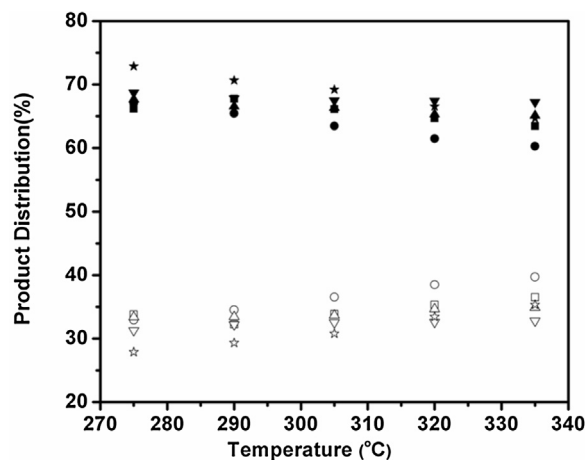
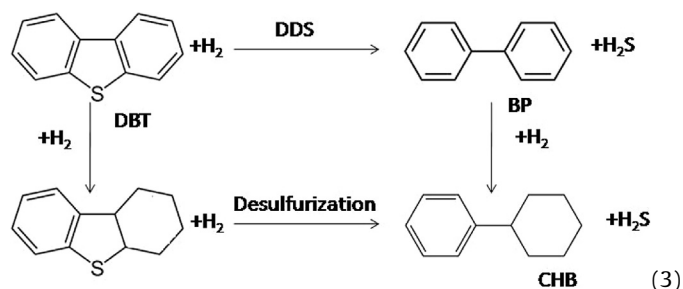


Fig. 9. Product distribution of biphenyl (BP) and cyclohexyl benzene (CHB) for HDS of DBT for different NiMo catalysts. (■) BP NiMo 1 (●) BP NiMo 2 (▲) BP NiMo 3 (▼) BP NiMo 4 (★) BP NiMo con1 (□) CHB NiMo 1 (○) CHB NiMo 2 (△) CHB NiMo 3 (▽) CHB NiMo 4 (☆) CHB con1.

The main products obtained during HDS for DBT were biphenyl (BP) and cyclohexyl benzene (CHB). It has been proposed that hydrodesulfurization of DBT follows two pathways: (i) direct desulfurization (DDS) in which the hydrogenolysis of sulfur bond takes place leading to the formation of biphenyl (BP); and (ii) desulfurization after hydrogenation of one of the aromatic rings followed by hydrogenolysis of the sulfur bond, leading to formation of cyclohexylbenzene (CHB) [48,49]. Reaction pathways for the hydrodesulfurization of dibenzothiophene is shown below:



The variation of the product distribution with temperature is shown in Fig. 9. For all the catalysts, the major product was BP. With an increase in temperature, there was a noticeable increase in the selectivity toward CHB. The product distribution indicates that the hydrogenation pathway dominates in the case of current colloidal synthesized catalysts compared to conventional wet impregnation method. This might be due to presence of higher number of rim sites. To check the effect of Ni on HDS activity two catalyst batches (NiMo 5 and NiMo 6) were prepared keeping MoO<sub>3</sub> loading constant. Similarly, to check the effect of Mo on HDS activity two catalyst batches (NiMo 7 and NiMo 8) were prepared keeping NiO constant. Figs. 10 and 11 show the effect of different NiO loading with respect to MoO<sub>3</sub> and different MoO<sub>3</sub> loading with respect to NiO on the HDS activity of the catalyst, respectively. The HDS activity result indicates that (Ni/Ni + Mo) ratio of ~0.3 possesses enhanced activity compared to other prepared catalysts which is in agreement with the previous reports [37].

The HDS activity was significantly affected by the size of the NiMo nanoclusters. A comparison of the conversions obtained with 2 nm NiMo metal oxide nanoclusters (obtained after 10 min reaction time) and 10 nm particles (NiMo B) formed after 30 min of reaction time is shown in Fig. 12. The metal loading for both the catalysts was kept the same. The activity of the larger size

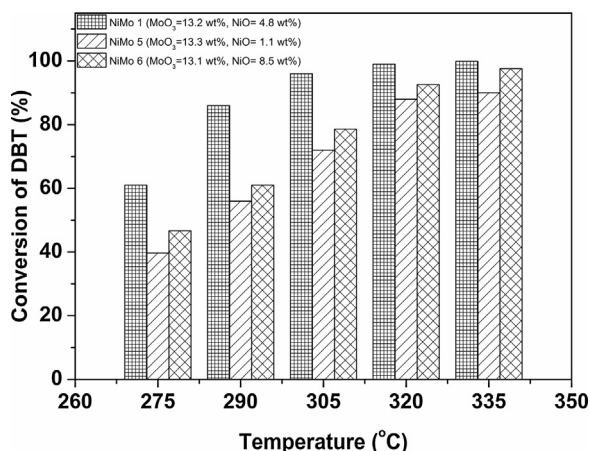


Fig. 10. Effect of reaction temperature and NiO content on the conversion of DBT ( $W/F_{A0} = 2.38 \times 10^2$  kg cat.h/kmol DBT,  $\text{MoO}_3$  wt%:  $13.2 \pm 0.1$ ).

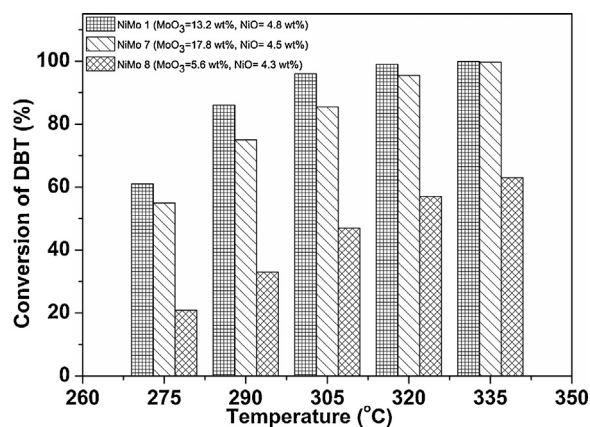


Fig. 11. Effect of reaction temperature and  $\text{MoO}_3$  content on the conversion of DBT ( $W/F_{A0} = 2.38 \times 10^2$  kg cat.h/kmol DBT,  $\text{NiO}$  wt%:  $4.5 \pm 0.3$ ).

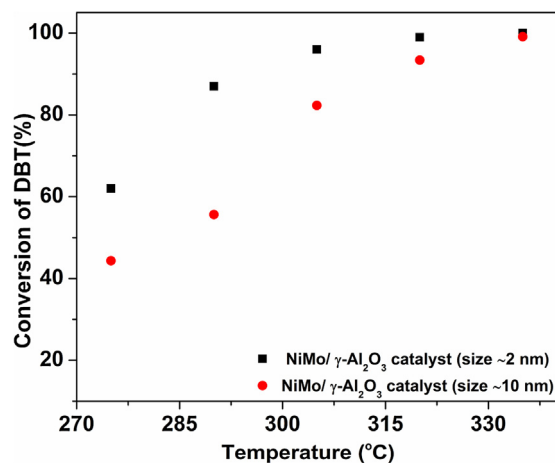


Fig. 12. Comparison of HDS activity of NiMo1 (size ~2 nm) and NiMo nanoparticles of size ~10 nm supported on  $\gamma\text{-Al}_2\text{O}_3$ .

particles was significantly lower most probably due to the lower metal dispersion.

### 3.3.1. Kinetics

To compare the performance of the different catalysts, the activities of the different catalysts were compared by calculating the rate constants at different temperatures. The rate equation for

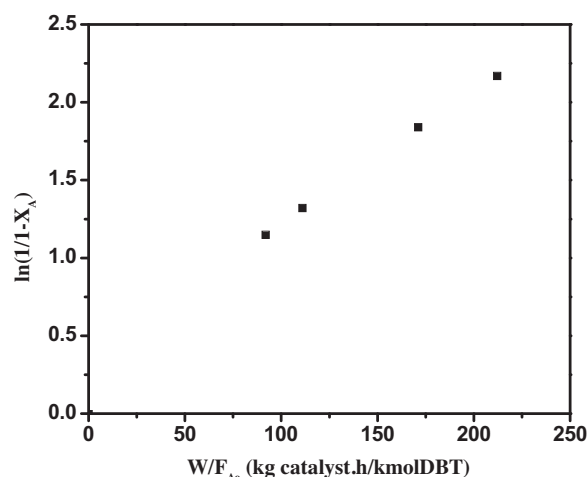


Fig. 13. Pseudo first order plot for hydrodesulfurization of DBT on NiMo1 catalyst (Temperature =  $290^\circ\text{C}$ ,  $W/F_{A0} = 2.38 \times 10^2$  kg cat.h/kmol DBT).

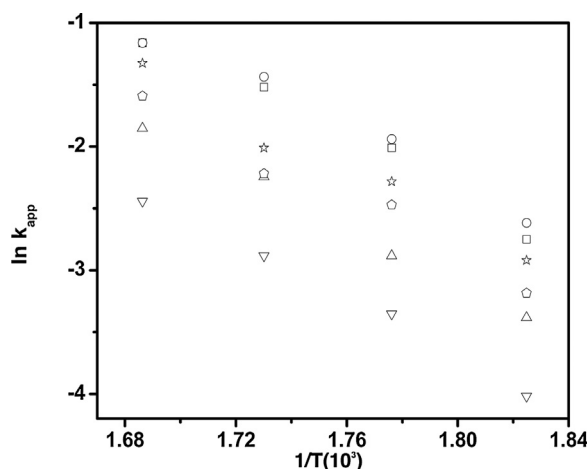


Fig. 14. Arrhenius plot for hydrodesulfurization reaction for the NiMo catalysts. (□) NiMo1 (○) NiMo2 (Δ) NiMo3 (▽) NiMo 4 (☆) NiMo con1 (○) NiMo con4.

pseudo-first order kinetics for a plug flow reactor can be expressed as follows:

$$\ln \left( \frac{1}{1 - X_A} \right) = k_{app} \frac{W}{F_{A0}} \quad (4)$$

where  $k_{app}$  is the apparent first order constant,  $F_{A0}$  is the inlet molar flow rate of DBT and  $W$  is the weight of the catalyst used for the reaction. To check the applicability of first-order kinetics, runs were taken at different flow rates of the feed at  $290^\circ\text{C}$  and 30 bar pressure. As shown in Fig. 13, the plot of  $\ln(1/(1 - X_A))$  vs.  $W/F_{A0}$  was linear, thus confirming that first-order kinetics could be used to represent the data.

The apparent rate constants at the different reaction temperatures were calculated on the basis of per unit mass of  $\text{MoO}_3$  present in the catalyst (Table 2). As expected, the rate constants increased with temperature. At identical conditions, the rate constants increased in the order  $\text{NiMo } 2 > \text{NiMo } 1 > \text{NiMo } 3 > \text{NiMo } 4 > \text{NiMo con1} > \text{NiMo con4}$ . This clearly shows that the catalysts prepared using colloidal synthesis had a higher activity compared to the conventional catalysts. The Arrhenius plots of the rate constants for the different catalysts are shown in Fig. 14. The activation energies for all the catalyst were in the range of 88–95 kJ/mol, which is in good agreement with the values of 79–129 kJ/mol for HDS of DBT on  $\text{NiMo}/\gamma\text{-Al}_2\text{O}_3$  reported in the literature [50–55].

**Table 2**Pseudo first-order rate constants for HDS of DBT for the different NiMo/ $\gamma$ -Al<sub>2</sub>O<sub>3</sub> catalysts.

Temperature (°C)	NiMo1 $k_{app}$ (m <sup>3</sup> /kgMoO <sub>3</sub> h)	NiMo2 $k_{app}$ (m <sup>3</sup> /kgMoO <sub>3</sub> h)	NiMo3 $k_{app}$ (m <sup>3</sup> /kgMoO <sub>3</sub> h)	NiMo4 $k_{app}$ (m <sup>3</sup> /kgMoO <sub>3</sub> h)	NiMo con1 $k_{app}$ (m <sup>3</sup> /kgMoO <sub>3</sub> h)	NiMo con4 $k_{app}$ (m <sup>3</sup> /kgMoO <sub>3</sub> h)
275	0.49	0.62	0.45	0.43	0.39	0.33
290	1.02	1.21	0.75	0.77	0.74	0.67
305	1.67	2.00	1.42	1.24	0.96	0.86
320	2.40	2.63	2.09	1.92	1.92	1.62

### 3.4. Analysis of spent catalyst

To check the stability of the catalyst, a longer duration run (24 h) were conducted using NiMo 1 or NiMo 2 catalyst at 290 °C and a  $W/F_{AO}$  of  $2.38 \times 10^2$  (kg cat.h/kmol of DBT). The results for NiMo1 are shown in Fig. S7 and there was no noticeable change in either the DBT conversion or the product selectivity over a period of 24 h. The spent catalyst after 24 h of operation was analyzed using TEM and Raman spectroscopy. The TEM image (Fig. S8) confirmed that there was no change in the particle size after the reaction suggesting the stability of prepared catalyst. Fig. S9 shows the Raman spectra of unsulfided and spent (NiMo con1 and NiMo 2) catalysts. Two broad peaks at 1350 cm<sup>-1</sup> and 1590 cm<sup>-1</sup>, are observed in the case of spent sulfide catalysts compared to unsulfided catalyst which can be attributed to amorphous carbon. There was no or minimal effect of this amorphous carbon on either the activity or selectivity for a test run of 24 h.

## 4. Conclusions

Monodispersed ultrasmall NiMo metal oxide nanoclusters of ~2 nm were successfully prepared by colloidal synthesis method using oleic acid and oleylamine as ligand. The size and composition of the metal oxide nanoclusters could be tailored by controlling the reaction parameters. The synthesized metal oxide nanoclusters supported on  $\gamma$ -Al<sub>2</sub>O<sub>3</sub> showed higher catalytic activity for HDS of dibenzothiophene in comparison to catalyst prepared using conventional impregnation method. The enhanced catalytic activity is most probably due to the smaller slab length of the nanoclusters, which results in higher number of HDS active edge atoms. The catalysts prepared using colloidal synthesis are more easily reducible in comparison to catalyst prepared using colloidal synthesis. Further, the catalyst did not exhibit any deactivation during the test run of 24 h suggesting the stability of the catalysts.

## Acknowledgments

The financial support provided by Chevron Corporation, USA and Hindustan Petroleum Corporation Limited, Mumbai for this study is gratefully acknowledged.

## Appendix A. Supplementary data

Supplementary data associated with this article can be found, in the online version, at <http://dx.doi.org/10.1016/j.apcatb.2015.12.013>.

## References

- [1] C. Song, X. Ma, Appl. Catal. B 41 (2003) 207–238.
- [2] K.K. Sarda, A. Bhandari, K.K. Pant, S. Jain, Fuel 93 (2012) 86–91.
- [3] Q. Gao, T.N.K. Ofosu, S.-G. Ma, V.G. Komvokis, C.T. Williams, K. Segawa, Catal. Today 164 (2011) 538–543.
- [4] P.G. Moses, B. Hinnemann, H. Topsøe, J.K. Nørskov, J. Catal. 268 (2009) 201–208.
- [5] Y. Villasana, F. Ruscio-Vanalesti, C. Pfaff, F.J. Méndez, M.Á. Luis-Luis, J.L. Brito, Fuel 110 (2013) 259–267.
- [6] A.M. Venezia, V. La Parola, V. Nicolì, G. Deganello, J. Catal. 212 (2002) 56–62.
- [7] R.M. Navarro, P. Castaño, M.C. Álvarez-Galván, B. Pawelec, Catal. Today 143 (2009) 108–114.
- [8] T. Klimova, P.M. Vara, I.P. Lee, Catal. Today 150 (2010) 171–178.
- [9] H. Nava, J. Espino, G. Berhault, G. Alonso-Núñez, Appl. Catal. A 302 (2006) 177–184.
- [10] R. Huirache-Acuna, G. Alonso-Núñez, F. Paraguay-Delgado, J. Lara-Romero, G. Berhault, E. Rivera-Muñoz, Catal. Today 250 (2015) 28–37.
- [11] H. Berit, M. Poul Georg, K.N. Jens, J. Phys.: Condens. Matter 20 (2008) 064236.
- [12] S.L. González-Cortés, S. Rugmini, T. Xiao, M.L.H. Green, S.M. Rodulfo-Baechler, F.E. Imbert, Appl. Catal. A 475 (2014) 270–281.
- [13] R. Huirache-Acuña, B. Pawelec, C.V. Loricera, E.M. Rivera-Muñoz, R. Nava, B. Torres, J.L.G. Fierro, Appl. Catal. B 125 (2012) 473–485.
- [14] E. Rodríguez-Castellón, A. Jiménez-López, D. Eliche-Quesada, Fuel 87 (2008) 1195–1206.
- [15] R. Shafi, G.J. Hutchings, Catal. Today 59 (2000) 423–442.
- [16] V. Rabarihoela-Rakotovo, S. Brunet, G. Perot, F. Diehl, Appl. Catal. A 306 (2006) 34–44.
- [17] G.M. Esquivel, J. Ramírez, A. Gutiérrez-Alejandro, Catal. Today 148 (2009) 36–41.
- [18] D. Gao, A. Duan, X. Zhang, Z. Zhao, E. Hong, J. Li, H. Wang, Appl. Catal. B 165 (2015) 269–284.
- [19] A. Duan, T. Li, Z. Zhao, B. Liu, X. Zhou, G. Jiang, J. Liu, Y. Wei, H. Pan, Appl. Catal. B 165 (2015) 763–773.
- [20] T.G. Kaufmann, A. Kaldor, G.F. Stuntz, M.C. Kerby, L.L. Ansell, Catal. Today 62 (2000) 77–90.
- [21] D. Genuit, P. Afanasiev, M. Vrinat, J. Catal. 235 (2005) 302–317.
- [22] F. Liu, S. Xu, L. Cao, Y. Chi, T. Zhang, D. Xue, J. Phys. Chem. C 111 (2007) 7396–7402.
- [23] H.A. Al-Megren, Arab. J. Sci. Eng. 34 (2008) 55–66.
- [24] B. Yoosuk, C. Song, J.H. Kim, C. Ngamcharussrivichai, P. Prasassarakich, Catal. Today 149 (2010) 52–61.
- [25] D. Barkhuizen, I. Mabaso, E. Viljoen, C. Welker, M. Claeys, E. van Steen, J.C.Q. Fletcher, Pure Appl. Chem. 78 (2006) 1759–1769.
- [26] V. Baglio, A.S. Aricò, A. Stassi, C. D'Urso, A. Di Blasi, A.M.C. Luna, V. Antonucci, J. Power Sources 159 (2006) 900–904.
- [27] W.G. Menezes, L. Altmann, V. Zielasek, K. Thiel, M. Bäumer, J. Catal. 300 (2013) 125–135.
- [28] M. Shah, Q.X. Guo, Y. Fu, Catal. Commun. 65 (2015) 85–90.
- [29] A. Meffre, V. Iablokov, Y. Xiang, R. Barbosa, P.F. Fazzini, V. Kelsen, N. Kruse, B. Chaudret, Catal. Lett. 145 (2014) 373–379.
- [30] Y. Yin, A.P. Alivisatos, Nature 437 (2005) 664–670.
- [31] K. Na, Q. Zhang, G. Somorjai, J. Clust. Sci. 25 (2014) 83–114.
- [32] S. Sun, C.B. Murray, D. Weller, L. Folks, A. Moser, Science 287 (2000) 1989–1992.
- [33] X. Wang, J. Stöver, V. Zielasek, L. Altmann, K. Thiel, K. Al-Shamery, M. Bäumer, H. Borchert, J. Parisi, J. Kolny-Olesiak, Langmuir 27 (2011) 11052–11061.
- [34] C. Bock, C. Paquet, M. Couillard, G.A. Botton, B.R. MacDougall, J. Am. Chem. Soc. 126 (2004) 8028–8037.
- [35] U.T. Turaga, C. Song, Catal. Today 86 (2003) 129–140.
- [36] Y. Li, Y. Dai, X.-k. Tian, Catal. Lett. 145 (2015) 1837–1844.
- [37] M. Sun, J. Adjaye, A.E. Nelson, Appl. Catal. A 263 (2004) 131–143.
- [38] W. Huang, Q. Hua, T. Cao, Catal. Lett. 144 (2014) 1355–1369.
- [39] D. Ferdous, A.K. Dalai, J. Adjaye, Appl. Catal. A 260 (2004) 137–151.
- [40] D. Valencia, T. Klimova, Appl. Catal. B 129 (2013) 137–145.
- [41] D. Valencia, T. Klimova, Catal. Today 166 (2011) 91–101.
- [42] D. Zhang, A. Duan, Z. Zhao, G. Wan, Z. Gao, G. Jiang, K. Chi, K.H. Chuang, Catal. Today 149 (2010) 62–68.
- [43] B.M. Vogelaar, P. Steiner, A. Dick van Langeveld, S. Eijssbouts, J.A. Moulijn, Appl. Catal. A 251 (2003) 85–92.
- [44] I. Mochida, K.-H. Choi, Current progress in catalysts and catalysis for hydrotreating, in: Practical Advances in Petroleum Processing, Springer, New York, 2006, pp. 257–296.
- [45] M. Daage, R. Chianelli, J. Catal. 149 (1994) 414–427.

- [46] G. Berhault, M. Perez De la Rosa, A. Mehta, M.J. Yácaman, R.R. Chianelli, *Appl. Catal. A* 345 (2008) 80–88.
- [47] R. Nava, A. Infantes-Molina, P. Castaño, R. Guil-López, B. Pawelec, *Fuel* 90 (2011) 2726–2737.
- [48] V. Lamure-Meille, E. Schulz, M. Lemaire, M. Vrinat, *Appl. Catal. A* 131 (1995) 143–157.
- [49] M. Houalla, D.H. Broderick, A.V. Sapre, N.K. Nag, V.H.J. de Beer, B.C. Gates, H. Kwart, *J. Catal.* 61 (1980) 523–527.
- [50] L.E. Kallinikos, A. Jess, N.G. Papayannakos, *J. Catal.* 269 (2010) 169–178.
- [51] F. Dumeignil, J.-F. Paul, E. Veilly, E.W. Qian, A. Ishihara, E. Payen, T. Kabe, *Appl. Catal. A* 289 (2005) 51–58.
- [52] T. Kabe, A. Ishihara, Q. Zhang, *Appl. Catal. A* 97 (1993) L1–L9.
- [53] D. Ferdous, A.K. Dalai, J. Adjaye, *Ind. Eng. Chem. Res.* 45 (2005) 544–552.
- [54] T. Song, Z. Zhang, J. Chen, Z. Ring, H. Yang, Y. Zheng, *Energy Fuels* 20 (2006) 2344–2349.
- [55] P. Steiner, E.A. Blekkan, *Fuel Process. Technol.* 79 (2002) 1–12.